Facet-preferential reduction of hematite nanocrystals by *Shewanella oneidensis* MR-1: An iron isotope tracer study

Jian Hua [a,b,c], Chunhua Feng [d], Jing Sun [b], Fei Wu [b], Feng Wu [a,**], Chengshuai Liu [b,c,*]

[a] *School of Resources and Environmental Science, Wuhan University, Wuhan 430079, China*
[b] *State Key Laboratory of Environmental Geochemistry, Institute of Geochemistry, Chinese Academy of Sciences, Guiyang 550081, China*
[c] *National-Regional Joint Engineering Research Center for Soil Pollution Control and Remediation in South China, Guangdong Key Laboratory of Integrated Agro-environmental Pollution Control and Management, Institute of Eco environmental and Soil Sciences, Guangdong Academy of Sciences, Guangzhou 510650, China*
[d] *School of Environment and Energy, South China University of Technology, Guangzhou 510006, China*

ARTICLE INFO

ABSTRACT

Coexistence of crystals with multiple facets on an individual particle or different crystals is prevalent in real environments. However, the reduction efficiency of individual crystal facets in facet-combined system is still enigmatic. This study aimed to determine the reduction efficiencies of different facets of hematite by *Shewanella oneidensis* MR-1. An iron isotope tracer was used to distinguish Fe(II) produced from reduction of the combined and separate hematite {001} and {100} facets, i.e., Hem {001} nanoplates and Hem {100} nanorods. Hem {001} nanoplates was reduced 1.8 times more significantly than Hem {100} nanorods when the two facets combined, whereas Hem {001} nanoplates was reduced only 1.2 times more significantly than Hem {100} nanorods in separate reactors. Initial $\sim$ 72% and final $\sim$ 63% of reduced atoms from Hem {001} nanoplate demonstrated the facet-preferential reduction of hematite crystal when the facets combined. The pseudo-first-order rate constants (*k*) of reduced Fe(II) for Hem {001} nanoplates and {100} nanorods were 3.2 and 2.0 $\times$ 10^{-2} d^{-1}, respectively. We attributed the more efficient reduction of Hem {001} nanoplates than Hem {100} nanorods to their differences in surface hydroxyl groups, surface charges, ligand-bound conformation and steric effects. These findings provide new insights into microbe-mineral interaction based on the crystal facet and the overall role of Fe oxides nanocrystals in the environments.

1. Introduction

Iron(III) oxides serve as the terminal electron acceptors in dissimilatory iron(III) reduction (DIR) processes that play an important role in Fe biogeochemical cycle and the associated fate and transport of vital elements (e.g., C, N, and P) (Colombo et al., 2014; Furukawa and Dale, 2013; Murray and Hesterberg, 2006; Roden and Urrutia, 2002; Van Cleemput, 1998; Weber et al., 2006; Wolf et al., 2009). Electrons that originate from intracellular catabolism are transferred to cell surface-localized c-type cytochromes, which catalyze the extracellular electron transfer for the reduction of Fe(III) via different pathways, including direct contacts, nanowires, and electron shuttles (Kappler et al., 2021; Melton et al., 2014). Recently, Fe mineral morphologies, including surface defects, crystallinity and particle sizes, were reported to impact the reduction efficiency of Fe(III)-reducing bacteria (Bose et al., 2009;

Cutting et al., 2009; Liu et al., 2016; Notini et al., 2019). In soil and groundwater systems, the different geochemical conditions can result in different Fe mineral morphologies and further alter the dominant exposed facets of Fe oxides (Cornell and Schwertmann, 2004; Huang et al., 2018; Lv et al., 2018; Zong et al., 2019). The types and proportions of dominant exposed facets have been identified to dominate the biogeochemical behavior of Fe oxides, due to their unique surface and intrinsic structures (Hu et al., 2021; Huang et al., 2016; Huang et al., 2018; Lv et al., 2018; Yang et al., 2011). However, there are limited studies on the reactivity of exposed facets in DIR processes.

Hematite (α-Fe$_2$O$_3$), the most thermodynamically stable Fe oxide on Earth's surface, has diverse crystal morphologies, such as well-defined platy crystals and spherical crystals (Carbone et al., 2005; Cornell and Schwertmann, 2004; Echigo et al., 2013). Hematite, therefore, is an ideal Fe(III) oxide for exploring the reduction efficiency of different

---

* Corresponding author at: State Key Laboratory of Environmental Geochemistry, Institute of Geochemistry, Chinese Academy of Sciences, Guiyang 550081, China.
** Corresponding author.
E-mail addresses: fengwu@whu.edu.cn (F. Wu), liuchengshuai@vip.gyig.ac.cn (C. Liu).

facets in crystals. The commonly exposed facets of hematite grain are {001}, {012} and {110} (Mackrodt et al., 1987; Noerpel et al., 2016). In previous studies, two classical hematite single crystals that are structurally well-defined, hematite {100} and {001} facets (Huang et al., 2018; Kerisit, 2011) (referred to hereafter as Hem {001} nanoplate and Hem {100} nanorod), were utilized to react with Fe(III)-reducing bacteria, respectively (Hu et al., 2020; Hu et al., 2021). The results showed that the structural Fe(III) of Hem {001} nanoplate were more easily reduced than that of Hem {100} nanorod owing to its higher conductivity, more surface reaction sites, and more oxidizing surface (Hu et al., 2020; Hu et al., 2021). Nonetheless, although these differences in hematite nanocrystals have the potential to lead to a facet-preferential reduction upon the crystal facets combined, it has so far remained a mystery.

The reactions at mineral–water interfaces are central of aqueous reactivity in natural waters, soils, and sediments (Hochella, 2013; Putnis, 2014; Yanina and Rosso, 2008). All of these fundamental reaction processes, e.g., adsorption/desorption (Jiang et al., 2020; Mei et al., 2020), interfacial electron transfer (Joshi et al., 2017; Yanina and Rosso, 2008), and precipitation/dissolution (Liu et al., 2021; Namgung et al., 2014), are strongly determined by the specific mineral facets available to aqueous solutions. Therefore, it is of significance to understand the interfacial reactions on individual crystallographic mineral facets. Hematite nanocrystals with high mobility and can be transported to subsurface (Luo et al., 2017), such that the microbially mediated reduction of hematite nanocrystals frequently occurs in the subsurface soils and groundwater. The crystal structure of hematite nanocrystals is generally anisotropic (Cornell and Schwertmann, 2004; Taylor et al., 2019), and the enclosed facets of individual particles will inherently expose two or more distinct sets of surface atomic structures. It is well established that coexistence of crystals with multiple facets on an individual particle or different crystals is prevalent in soil and groundwater systems. Therefore, when assessing the reactivity and bioavailability of Fe oxide nanocrystals in real environments, the effects of the coexistence of multiple crystal facets on the bioreduction reactivity of individual crystal facets should be considered.

Different facets of an individual particle or different crystals are interactive and interdependent, on account of the competitive effect between different facets and interfacial electron transfer via bulk conduction (Soltis et al., 2017; Yanina and Rosso, 2008; Zarzycki et al., 2015). The coexisted crystals with multiple facets are believed to have a unique biochemical reactivity that is different from the isolated single crystals. The distribution of adsorbed Fe(II) on individual facet of a hematite particle was recorded, and the results suggested a stronger selectivity of Fe(II) adsorption onto hematite {001} facet relative to hematite {100} and {012} facets (Taylor et al., 2019). Two isolated single crystals of hematite were also employed to react with Fe(II) separately, however, it was reported that hematite {012} facet exhibits a stronger reactivity than hematite {001} facet (Wu et al., 2021). The interaction of crystal facets may be responsible for the difference in the reactivity of hematite facets to Fe(II) between Taylor et al. (2019) and Wu et al. (2021) (Taylor et al., 2019; Wu et al., 2021). Therefore, we hypothesize that the interaction of crystal facets might determine the biogeochemical reactivity of mineral crystals (Taylor et al., 2019).

To test our hypothesis, the present study explored the reduction efficiency of hematite facets in the mixture when they are exposed to Fe(III)-reducing bacteria in the facet-combined system. Two architectural hematite nanocrystals with different dominant exposed facets were synthesized. Moreover, we used the isotope-labeled hematite nanocrystals, i.e., isotopically natural hematite and ^{56}Fe-enriched hematite, to differentiate Fe(II) produced from the reduction of each hematite facet by *Shewanella oneidensis* MR-1. New insights into the facet-preferential reduction of hematite nanocrystals and interplays of crystal facets in the facet-combined system are presented. The findings of this study help us to better understand the bio-reducibility of Fe minerals with different exposed facets in the environments.

2. Materials and methods

2.1. Chemicals and materials

All of the chemical reagents used in this study were of analytical grade and purchased from Sigma-Aldrich without further purification, except for ^{56}Fe-enriched zerovalent iron (99.94% purity) from Isoflex. All reagent stocks were obtained by dissolving the corresponding solids into deionized water (18.2 MΩ•cm). *Shewanella oneidensis* MR-1 strain was gained from laboratory stocks. The Hem {001} nanoplates and Hem {100} nanorods were synthesized based on a modified solvothermal method according to previous studies (Chen et al., 2010; Li et al., 2009). More details about the synthesis procedure were in Text S1 of the supporting information (SI).

2.2. Synthesis of isotope-labeled hematite nanocrystals and characterization

Isotope-labeled hematite nanocrystals were synthesized from zerovalent Fe metals with unique isotope compositions. To be specific, the isotopically natural hematite nanocrystals (referred to as ^{NA}Hem) with $2.30 \pm 0.01\%$ of ^{57}Fe were prepared from isotopically natural zerovalent iron, while the ^{56}Fe-enriched hematite nanocrystals (referred to as ^{56}Hem) with virtually no ^{57}Fe were prepared from ^{56}Fe-enriched zerovalent iron. The Fe metal was firstly dissolved in 6 M HCl, from which a ~ 0.5 M Fe(II) stock was obtained. Then excess H_2O_2 (3 mL of 30% H_2O_2) was added. The volume of resulting Fe(III) stock (pH ≈ 0.5) was reduced to ~ 2 mL through heating in a water bath. To avoid the hydrolysis between dissolved Fe(III) and water molecules, pH of the solution was maintained at pH < 1 by the addition of concentrated HCl throughout the heating period. Note that the subsequent synthesis procedures can increase the pH values of solution because of the addition of ultrapure water and other chemical agents (e.g., ethanol or 1, 2-diaminopropane). Moreover, hematite is the thermodynamically most stable Fe mineral in soil (Barton et al., 2012), and therefore, the corrosion or partial dissolution of hematite nanocrystals during the synthesis were negligible in this study.

The synthesized hematite nanocrystals were characterized by X-ray diffraction (XRD) (D2 Phaser, Bruker). The XRD data were collected over 2-theta range from 10 to 100° using Cu Kα radiation. The morphology of the hematite was measured with a field emission scanning electron microscopy (SEM) (Sigma 300, ZEISS) and a high-resolution transmission electron microscopy (HRTEM) (FEI Tecnai G2 F20 TEM, Thermo Fisher Scientific). Both SEM and HRTEM images were processed using Digital Micrograph software. ^{57}Fe Mössbauer spectra were collected on a spectrometer WSS-10 (Wissel GmbH) that operated at 13 K (SHI-850, Janis Research). FTIR, XPS, and BET specific surface area analyses were also conducted with detailed procedures provided in SI Text S2. In addition, the details of surface charge density measurements were provided in SI Text S3.

2.3. Microbially mediated reduction experiments

All the reagents were autoclaved (120 °C for 20 mins) and purged by ultrapure N_2 (99.999% purity) for 2 h before equilibration inside an anaerobic chamber for 24 h or longer. The *Shewanella oneidensis* MR-1 cells were aerobically cultured in 100 mL serum bottles with Luria-Bertani medium (LB, 10 g L^{-1} tryptone, 5 g L^{-1} yeast extract, and 10 g L^{-1} NaCl) on a rotary shaker at 180 rpm for 16 h at 30 °C in the dark. Once the culture entered the log phase (OD$_{600}$ 2.4–2.8), cells were harvested by centrifugation at 8000 rpm for 5 mins at 4 °C. To remove the residual LB medium, the resuspension was washed 5 times using sterile 4-(2-hydroxyethyl)-1-piperazineethanesulfonic acid HEPES plus 30 μM phosphate culture medium (Royer et al., 2002). The resulting cell pellets were then resuspended in a N_2-purged culture medium and stored at 4 °C.
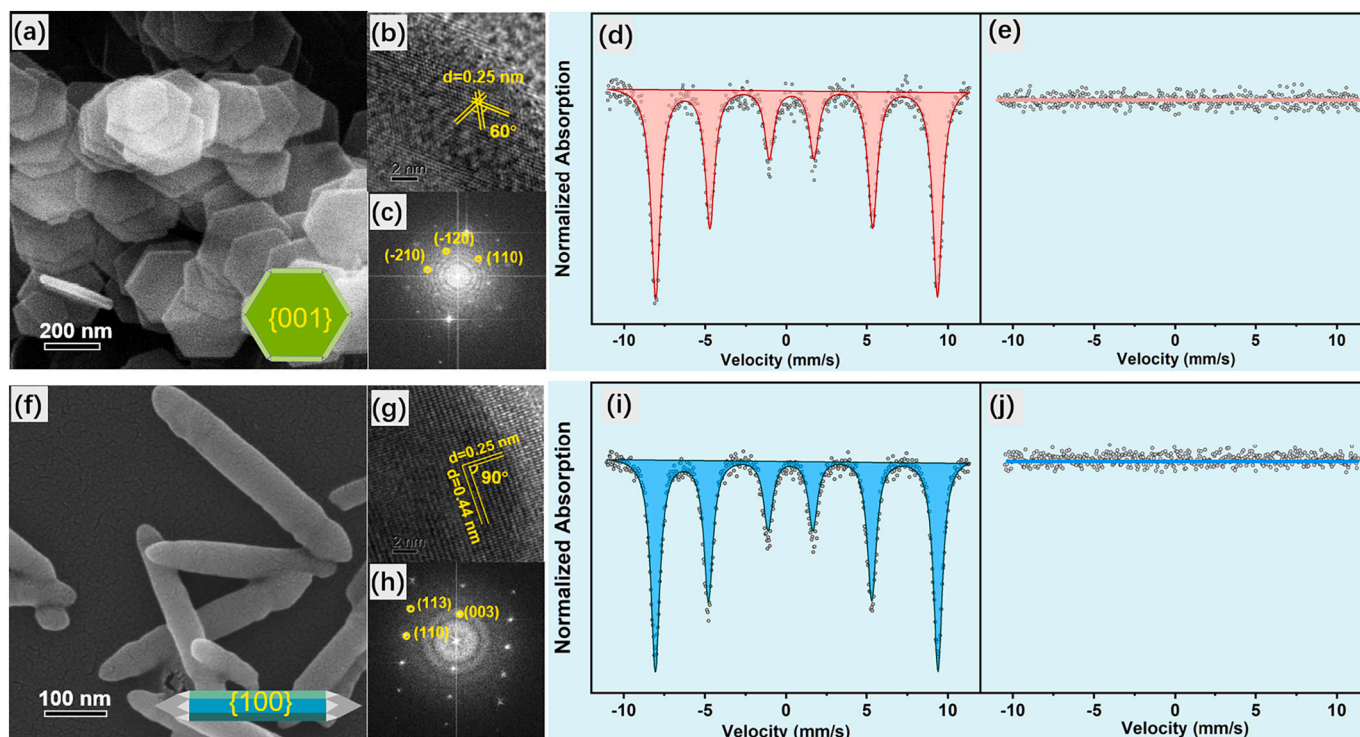
Fig. 1. The SEM images (a, f), HRTEM images (b, g), FFT patterns (c, h). Insets in images (a) and (f) are schematic drawings of a nanoplate and a nanorod. 13 K Mössbauer spectra of isotope-labeled hematite nanocrystals with (d) [NA]Hem {001} nanoplate; (e) [56]Hem {001} nanoplate; (i) [NA]Hem {100} nanorod; and (j) [56]Hem {100} nanorod.

The batch experiments of microbially mediated reduction were conducted using 50 mL sterile serum bottles in triplicate. Each serum bottle contained 25 mL mixed suspension including 10 mM sodium lactate, 0 or $\sim 10^8$ cells mL^{-1} of *Shewanella oneidensis* MR-1 cells, anaerobic culture medium, 50 mM of HEPES buffer, 0 or 10 μM of anthraquinone-2,6-disulfonate (AQDS) and 1 or 2 g L^{-1} of hematite nanocrystals. The suspension was adjusted to pH 7.0 with 0.1 M NaOH or HCl under the optimal conditions of *Shewanella oneidensis* MR-1 cell (Weihe et al., 2019). All the procedures were performed in an anaerobic chamber (93% N$_2$ and 7% H$_2$, Coy) where the oxygen level was controlled to <1 ppm by circulating the atmosphere over a Pd catalyst, which was confirmed with an oxygen sensor (CAM-12, Coy). The serum bottles were sealed with butyl rubber stoppers and incubated on an orbital shaker at 180 rpm in the dark at 30 °C. The duration of the experiment was 30 days, during which the serum bottles were opened for subsampling at different time intervals. During subsampling, a homogeneous 3 mL aliquot was removed from each bottle and centrifuged at 9500 rpm for 10 mins. The subsampling procedures were believed to posse a negligible effect on the system's Fe mass balance (Hu et al., 2020; Notini et al., 2019). The supernatants were acidified with 2% HCl. The solids were extracted with 3 mL of 0.6 M HCl for 12 h (Luo et al., 2017), centrifuged and filtered to 0.22 μm. The Fe(II) and total Fe concentrations in the supernatants and the extractants were quantified based on the 1,10-phenanthroline method (Tamura et al., 1974). Additional solid samples used for Mössbauer, SEM, and HRTEM analyses were collected by filtering suspensions through syringe filters and air drying inside the anaerobic chamber.

2.4. Isotope-labeled microbially mediated reduction

In the present study, ^{56}Fe and ^{NA}Fe were applied to differentiate Hem {001} nanoplate and Hem {100} nanorod. Four different treatments were carried out in triplicate as following: (1) a mix of 25 mg ^{56}Hem {001} nanoplates and 25 mg ^{NA}Hem {100} nanorods, (2) 25 mg ^{NA}Hem {001} nanoplates and 25 mg ^{56}Hem {100} nanorods, (3) 12.5 mg ^{56}Hem {001} nanoplates and 37.5 mg ^{NA}Hem {100} nanorods, and (4) 37.5 mg ^{56}Hem {001} nanoplates and 12.5 mg ^{NA}Hem {100} nanorods. A series of mass ratios (i.e., 0.5, 1, and 2) of ^{56}Hem {001} nanoplate and ^{NA}Hem {100} nanorod were set for exploring the effects of the facets mixing on the facet-preferential reduction in the present study. Except for the isotope composition and mixing proportion of hematite nanocrystals, these treatments were carried out according to the section of *Microbially Mediated Reduction Experiments*.

2.5. Analyses of Fe isotope compositions

Iron isotopic composition were measured using a quadrupole inductively coupled plasma mass spectrometer (ICP-MS, NexION 300D, Perkin-Elmer), operating in a collision cell mode. A collision cell gas (93% He and 7% H$_2$) was used to eliminate the isobaric interferences (ArO$^+$ and ArN$^+$). All solutions were diluted to roughly 1 μM Fe with 2% HNO$_3$. Fe isotope fractions were computed by multiplying the numbers in each isotope channel by the sum of all four channels' total counts (masses of 54, 56, 57, and 58) (Frierdich et al., 2015; Handler et al., 2009; Handler et al., 2014).

3. Results and discussion

3.1. Mineralogical and morphological characteristics of isotope-labeled hematite nanocrystals

XRD confirmed the identity of hematite (α-Fe$_2$O$_3$, JCPDS No. 99–0060) without any impurity and its high crystallinity (Fig. S1). The strongest peaks in XRD pattern, e.g., (104) peak for Hem {001} nanoplate and (110) peak for Hem {100} nanorod, represented the more dominant crystal development of Hem {100} nanoplate in *c* direction and the more dominant crystal development of Hem {001} nanoplate in *a-b* direction, respectively (Chan et al., 2015; Cornell and Schwertmann,
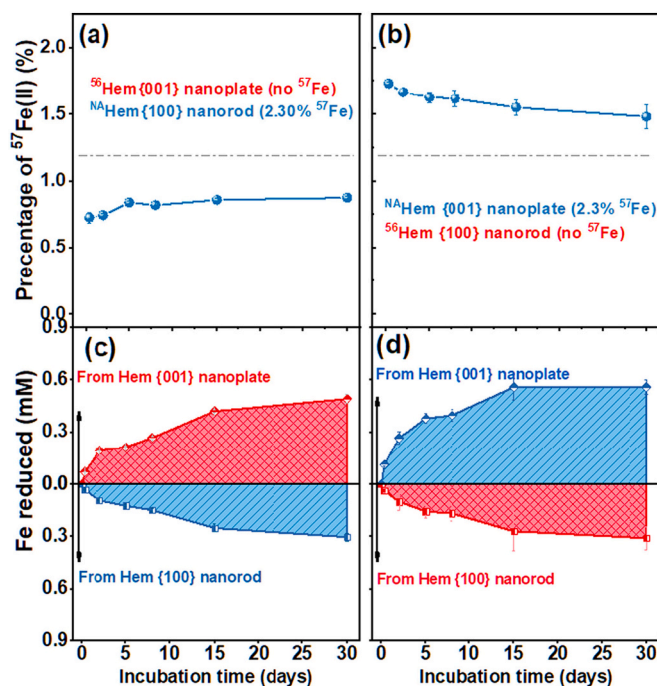
Fig. 2. Percentage of ^{57}Fe isotope in reduced Fe(II) fraction (a and b) and the origin of the reduced Fe(II) (c and d) of the microbially reduced Fe from reactors containing an equal mix of isotopic-labeled Hem {001} nanoplate and Hem {100} nanorod. In panel (a) and (c), Hem {001} nanoplate is labeled with the ^{56}Fe isotope, while in panel (b) and (d), Hem {100} nanorod is labeled with the ^{56}Fe isotope. Values for data points represent the mean of triplicate reactions, error bars are the standard deviation of triplicate measurements, and error bars not visible are smaller than symbols.

2004). FTIR spectra also showed that no residual organic impurities existed on hematite powders after calcination at 400 °C for 2 h (Fig. S2). The SEM and TEM images showed the plate-like and rod-like morphologies of the two hematites (Fig. 1a, f, and S3), which were composed of hexagonal nanoplate and hexagonal nanorod as reported previously (Huang et al., 2018; Lv et al., 2018). HRTEM and fast-Fourier transform (FFT) patterns disclosed that the lattice fringe of the hexagonal nanoplates (i.e., Hem {001} nanoplate) was 0.25 nm with an interfacial angle of 60°, which was consistent with structural features of (110), (−120), and (−210) lattice planes along the [001] zone axis (Fig. 1b and c). The exposed {001} and {113} facets occupied ∼ 87.6% and ∼ 12.4% of total surface area, which were calculated according to the mean diameter and thickness (261.45 and 18.61 nm) of the nanoplate (Fig. S4a and S4b). Additionally, the dominant exposed facets of hexagonal nanorod were enclosed by six equivalent {100} facets occupying ∼93.9% of the total surface area according to the mean length and width (498.58 and 67.53 nm) (Fig. 1g, h, S4c, and S4d). Therefore, the dominant exposed facets of synthetic hematite nanoplate and nanorod were Hem {001} nanoplate and Hem {100} nanorod, respectively (insets in Fig. 1a and f). Mössbauer spectra were used to verify the intended isotope compositions of hematite. While there were no absorption peaks in ^{56}Fe-enriched hematite samples (Fig. 1e and j), a sextet of hematite signals were observed in the isotopically natural hematite samples (center shift (δ) = 0.47 mm s^{-1}, quadrupole splitting (Δ) = 0.27 mm s^{-1}, Fig. 1d and i).

3.2. Microbially mediated reduction of isotope-labeled Hem {001} nanoplate and Hem {100} nanorod

The mixture with equal amounts of ^{56}Hem {001} nanoplate and ^{NA}Hem {100} nanorod was inoculated with *Shewanella oneidensis* MR-1 in the presence of electron shuttles (i.e., AQDS). All ^{57}Fe in the reactor was from ^{NA}Hem {100} nanorods, with the initial ^{57}Fe abundance being

1.19 ± 0.03% (dashed line in Fig. 2a). The temporal changes of ^{57}Fe abundance in aqueous and HCl-extracted Fe(II) can be used to track the origin of the reduced Fe during microbial respiration (Fig. 2a and Table S1). If ^{56}Hem {001} nanoplate and ^{NA}Hem {100} nanorod were reduced equally efficiently by *Shewanella oneidensis* MR-1 in the presence of AQDS, the isotopic abundance of total Fe(II) were expected to be maintained at ^{57}Fe = 1.19% throughout the experiments. Nevertheless, the ^{57}Fe isotopic abundance in the total Fe(II) fraction decreased to 0.73 ± 0.04% after 8 h incubation and then gradually increased to 0.88% ± 0.01% after 30 days (Fig. 2a). The ^{57}Fe isotopic abundance was significantly lower than the completely mixed value, i.e., 1.19%, which meant that more Fe(III) on ^{56}Hem {001} nanoplate was reduced than that on ^{NA}Hem {100} nanorod.

Nevertheless, preferential reduction of one isotope (i.e., isotopic fractionation) may have biased our data in this study. Isotopic fractionation occurs in many biological and geochemical processes and causes changes in Fe isotope composition (Boschker and Middelburg, 2002; Chanda et al., 2021; Crosby et al., 2005). Previous studies have reported that the DIR enhanced the reduction of lighter Fe isotopes (Boschker and Middelburg, 2002; Chanda et al., 2021). Thereby, the ^{56}Fe/^{54}Fe ratio of Fe reduced from Fe(III) oxide was lower than the value of initial Fe(III) oxide (Crosby et al., 2005; Johnson et al., 2005). Additionally, the direct electron exchange between aqueous Fe(II) and Fe(III) oxide could lead to the isotope fractionation, because Fe oxides preferentially absorb heavier isotopes that can further undergo electron transfer to form a new layer of mineral (Wu et al., 2010). Furthermore, the continuous interactions between Fe(II) and the neoformed Fe(III) layer could lead to further isotopic mixing (Reddy et al., 2015). Note that Hem {001} nanoplate was labeled with the lighter isotopes, therefore it may be favored by isotopic fractionation (Chanda et al., 2021; Crosby et al., 2005). The value of ^{56}Fe/^{54}Fe isotopic fractionation between aqueous Fe(II) and the solid Fe(III) oxide is approximately 3‰ (Crosby et al., 2005). In the present study, the ratio of ^{56}Fe/^{54}Fe in the completely mixed hematite nanocrystals (^{56}Fe/^{54}Fe$_{hematite}$) was 34.10%, whereas the ratio of ^{56}Fe/^{54}Fe in the solution Fe(II) (^{56}Fe/^{54}Fe$_{solution}$) was calculated as 43.79% after incubation for 30 days. Therefore, the value of ^{56}Fe/^{54}Fe isotopic fractionation (i.e., ^{56}Fe/^{54}Fe$_{solution}$ minus ^{56}Fe/^{54}Fe$_{hematite}$) was 9.7%, which is much larger than the ∼ 3‰. Consequently, the observed changes of Fe isotope abundance in this study are ascribed to the facet-preferential reduction of Hem {001} nanoplate, instead of the Fe isotope fractionation.

To further estimate whether the facet-preferential reduction of hematite nanocrystals is ascribed to the differences between two hematite nanocrystals or the selective use of one isotope, we reversed the isotope labeling of the Hem {001} nanoplate and Hem {100} nanorod and measured the isotopic composition in total Fe(II) fraction during microbial respiration. Hence, ^{NA}Hem {001} nanoplates and ^{56}Hem {100} nanorods were prepared and confirmed by Mössbauer spectra (Fig. 1a and g), and all ^{57}Fe present in the reactor was from ^{NA}Hem {001} nanoplate this time. The ^{57}Fe isotopic abundance in total Fe(II) fraction was 1.73 ± 0.01% after inoculation for 8 h, gradually reduced to 1.48% ± 0.09% over 30 days (Fig. 2b and Table S1) and still did not reach the completely mixed value of 1.19% at the end of the incubation. The relatively high ^{57}Fe isotope abundance suggested more Fe(II) produced from the reduction of ^{NA}Hem {001} nanoplate than that from ^{56}Hem {100} nanorod. As for both isotope experiments, the Fe(II) fraction reduced from Hem {001} nanoplates is larger than that reduced from Hem {100} nanorod. Switching the hematite isotope labels appeared to have no effect on the origin of Fe(II) formed from microbial respiration of the hematite facet mixture. Consequently, the effect of the isotope fractionation on the selective use of one isotope was believed to be negligible during the microbial reduction (Notini et al., 2019). Both experiments indicated that, in the combined system, Hem {001} nanoplate was preferentially reduced by *Shewanella oneidensis* MR-1 relative to Hem {100} nanorod, which was independent of the type of the hematite nanocrystal labeled with ^{57}Fe.
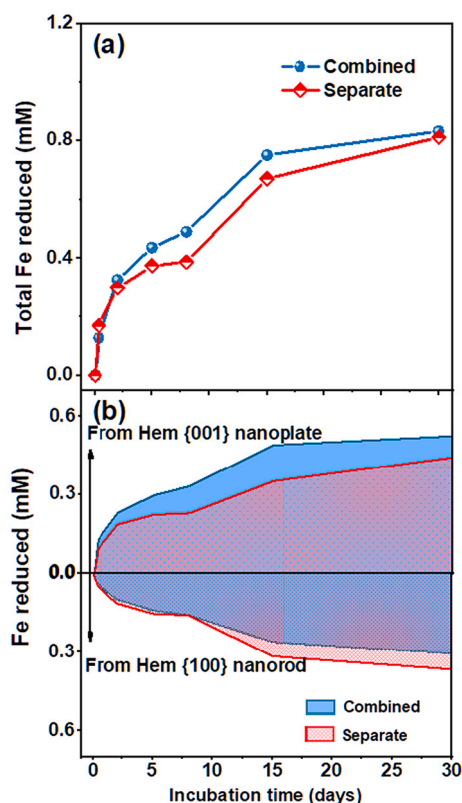
Fig. 3. Total Fe(II) reduced by microbial Fe(III) reduction (a) and the origin of the reduced atoms from the reduction of Hem {001} nanoplate and Hem {100} nanorod (b) when the two incubation was separate and combined.

To compare the two batch experiments with switched isotope labeling regardless of which hematite was labeled with ^{57}Fe, we calculated the amounts of Fe reduced from each hematite nanocrystal based on the ^{57}Fe abundance in total Fe(II) fraction. The specific calculation equations were shown in eq. 1–2. To convert the percentage of ^{57}Fe in the reduced atoms to the percentage of atoms arising from the ^{NA}Fe-labeled hematite facet we divided the abundance of ^{57}Fe per 0.023 (abundance of ^{57}Fe in our natural abundant samples). Then the amounts of reduced Fe atoms were calculated via multiplying the percentage of atoms reduced from each hematite facet by the total amount of Fe(II) (eq. 3–4). By this means, the amounts of reduced Fe(II) in both switched isotope experiments could be compared regardless of which hematite was labeled with ^{57}Fe (Fig. 2c and d, Table S2). In the two switched isotope experiments, the mean Fe(II) fractions produced from the reduction of Hem {001} nanoplates during microbial respiration were both ~ 72% initially and ~ 63% at the end (Table S2). The mean density of Fe(II) reduced from Hem {001} nanoplate and Hem {100} nanorod were ~0.53 mM and ~0.31 mM after 30 days, respectively (Fig. S5a). In addition, the pseudo-first-order rate constants (k) of Fe(II) generation were 3.2×10^{-2} d^{-1} for Hem {001} nanoplates and 2.0×10^{-2} d^{-1} for Hem {100} nanorods (Fig. S5b). Both these results suggested that Hem {001} nanoplates is more favorable for reduction than Hem {100} nanorods. This further proved that facet-preferential reduction of hematite nanocrystals should be ascribed to the differences between the hematite facets rather than isotopic fractionation.

$$P \text{ from } ^{NA}\text{Hem} = \frac{^{57}\text{Fe abundance of reduced Fe(II)}}{0.023} \tag{1}$$

$$P \text{ from } ^{56}\text{Hem} = 1 - \frac{^{57}\text{Fe abundance of reduced Fe(II)}}{0.023} \tag{2}$$

$$A \text{ from } ^{NA}\text{Hem} = P \text{ from } ^{NA}\text{Hem} \times \text{Total amount of Fe(II)} \tag{3}$$

$$A \text{ from } ^{56}\text{Hem} = P \text{ from } ^{56}\text{Hem} \times \text{Total amount of Fe(II)} \tag{4}$$

where P is percentage of reduced Fe atoms, A is amounts of reduced Fe atoms, 0.023 is the abundance of ^{57}Fe in natural abundant sample.

The surface area of Fe oxide has been reported to strongly impact its reactivity in biogeochemical processes (Roden and Urrutia, 2002; Roden and Zachara, 1996). However, the Hem {001} nanoplate and Hem {100} nanorod used in this study have similar surface areas of 13.4 m^2 g^{-1} and 11.8 m^2 g^{-1} based on BET isotherm using N$_2$ as adsorbate (Fig. S6). If the reduction of hematite nanocrystals were only a function of surface area, it would be 53.2% (13.4/ (13.4 + 11.8)) of the Fe(II) reduced from Hem {001} nanoplate and 46.8% (11.8/ (13.4 + 11.8)) reduced from Hem {100} nanorod. Instead, the initial ~ 72% and final ~ 63% of reduced atoms from Hem {001} nanoplate were observed (Fig. 2 and Table S2). Based on the findings above, we concluded that the facet-preferential reduction of hematite nanocrystals is not related to their surface areas but can instead be attributed to their internal properties.

3.3. Extents of hematite facet reduction (separate vs. combined)

To assess whether facet-preferential reduction of hematite nanocrystal in both switched isotope experiments was simply ascribable to the linear combination of the reduction of two hematite nanocrystals, the experiments where 1 g L^{-1} of each hematite nanocrystal in two separate bottles were conducted. Then we added the average concentration of Fe(II) produced from both hematite facets. The total Fe(II) reduced from the facet-separate system was compared with that from the facet-combined system (Fig. 3a and Table S3). After incubation for 30 days, the amounts of total Fe(II) were similar no matter the separate or combined reduction since both systems contained equal hematite density (1 g L^{-1} of Hem {100} nanorods plus 1 g L^{-1} of Hem {001} nanoplates). Nevertheless, there was a distinct difference between the fractions of Fe(II) reduced from Hem {001} nanoplates (area above the x-axis, Fig. 3b) and from Hem {100} nanorods (area below the x-axis, Fig. 3b). At the end of the experiments, the amounts of Fe atoms reduced from Hem {001} nanoplate were 1.2 times greater than that from Hem {100} nanorod (gray shaded area) when the two incubated separately, which is similar to previous studies (Hu et al., 2020; Hu et al., 2021). However, the amounts of Fe atoms reduced from Hem {001} nanoplate were 1.8 times greater than that from Hem {100} nanorod (blue shaded area) when the two hematite facets combined (Fig. 3b and Table S4). In addition, the initial rates of Fe(III) reduction (calculated from t = i to t = i + 1) in the facet-combined and -separate systems were also different (Fig. S7). The initial rate of Fe(III) reduced from Hem {001} nanoplate was 1.9 times greater than that from Hem {100} nanorod when the reduction happened separately (Fig. S7b). In comparison, the initial rate of Fe(III) reduced from Hem {001} nanoplate was 3.2 times greater than that of Hem {100} nanorod when the facets combined (Fig. S7a). Both the extent and initial rate of Fe(III) reduction indicated that Hem {001} nanoplate is more prone to reduction compared with Hem {100} nanorod in the facet-combined system.

After reduction for 30 days, both hematite nanocrystals had breakages and defects regardless of whether the incubation was separate or combined (Fig. S8), revealing that reductive dissolution of hematite nanocrystals occurred via microbially mediated corrosion of the solid surface. Nevertheless, due to the disordered sites and various types of breakages and defects, it is difficult to quantify the reduction extents of both hematite facets by the percentages of the breakages and defects on their surfaces (Eggleston et al., 2006; Taylor et al., 2019). Both SEM and Mössbauer spectroscopy found no secondary Fe mineral in all the experiments over 30 days (Fig. S8 and S9). In contrast, previous studies have reported the formation of vivianite and extracellular magnetite during the microbially mediated reduction of hematite (Luo et al., 2017; Notini et al., 2019).The absence of the vivianite phase in the present
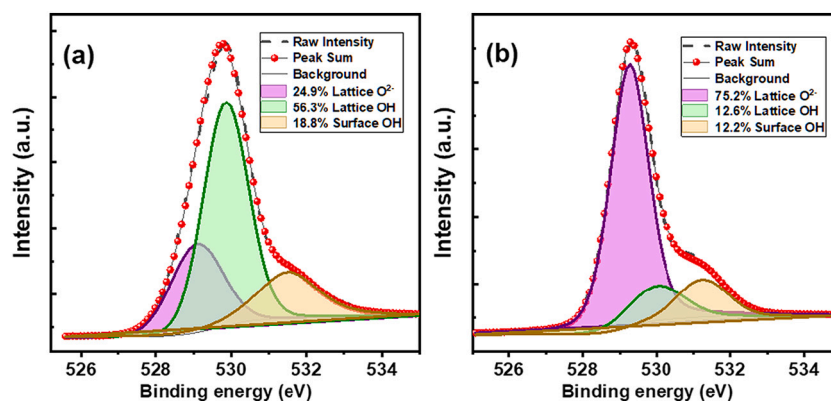
Fig. 4. O 1 s XPS spectra of (a) Hem {001} and (b) Hem {100}. The color lumps in the panels represent the percentage of each functional group based on peak fitting.

study could be explained by the low phosphate content in the culture medium (30 μM). In addition, the amount of reduced Fe atoms in both hematite nanocrystals was relatively low (approximately 0.8 mM), which probably hindered the formation of the extracellular magnetite phase.

The central role of biogeochemical reactivity of Fe oxide crystals in determining the efficiency of microbially mediated reduction is unrelated to the facet-separate or -combined incubation (Cutting et al., 2009; Notini et al., 2019). However, mineral morphology plays a critical role in impacting the efficiency of microbially mediated reduction. For instance, Fe oxide grains with more surface defects or lower crystallinity produce more Fe(II) during DIR processes (Eggleston et al., 2006; Notini et al., 2019). This means Fe(III) on the defective or poor crystalline surfaces has stronger reactivity than that on the perfect or crystalline surfaces (Notini et al., 2019). Similarly, in the present study, facet-preferential reduction of Hem {001} nanoplate in the faceted-combined system might be attributable to its stronger biogeochemical reactivity than Hem {100} nanorod. The pores and defects on both Hem {001} nanorod and Hem {100} nanoplate might accelerate the reductive dissolution of Fe atom by Fe(III)-reducing bacteria (Fig. S3). Note that the low surface area of both hematite nanocrystals (e.g., 13.4 and 11.8 $m^2 g^{-1}$) implied that the both hematite surfaces were very smooth and didn't get etched or partially dissolved during the synthesis (Fig. S6). Both the hematite single crystals have almost similar surface pores (Fig. S6), and there was no direct correlation between the defects and the crystal facets, thereby, in this study, the effects of defects on facet-preferential reduction were negligible.

The facet-preferential reduction on hematite nanocrystals can also be attributed to conductivity, resistance, and oxidizing surface as reported in the literatures (Hu et al., 2020; Hu et al., 2021). Moreover, the different reactivity of Hem {001} nanoplate and Hem {100} nanorod are probably related with the surface hydroxyl groups (Hu et al., 2020). The O 1 s peak fitting results of the XPS spectra indicated that surface hydroxyl group (-OH) on Hem {001} nanoplate was more abundant than that on Hem {100} nanorod (Fig. 4a and b, Table S5). The two higher energy peaks at 531.5 and 531.3 eV are assigned to hydroxyl groups (Fe–OH adsorbed) as a result of the adsorption and dissociation of water (Baltrusaitis et al., 2007; Hu et al., 2021; Wu et al., 2021). In addition, the experimental point of zero charge values of Hem {001} nanoplate and Hem {100} nanorod were 7.8 and 6.1, respectively (Fig. S10). Hem {001} nanorplate is more positive charged than Hem {100} nanorod because there were more surface hydroxyl groups on Hem {001} nanorplate. The Hem {001} nanoplate facet with more hydroxyl groups could provide more adsorption sites for electron shuttles (i.e., electron donor), accelerating the reduction of Hem {001} nanoplate by Fe(III)-reducing bacteria (Hu et al., 2020; Luetzenkirchen et al., 2013). Moreover, it has been reported that different from Hem {100} nanorod, ascorbic acid could form an inner-sphere bidentate mononuclear

complex on Hem {001} nanoplate surface, which facilitates the electron transfer between ascorbic acid and Hem {001} nanoplate (Huang et al., 2017a; Huang et al., 2017b). Since the structures of many organic electron shuttles (e.g., AH_2QDS) are similar to ascorbic acid (Larsen et al., 2006), the shuttle-mediated reduction of Fe(III) on Hem {001} nanoplate is also faster than that on Hem {100} nanorod. Moreover, Hem {001} nanoplate is of higher surface charge than Hem {100} nanorod (Fig. S10), such that AQDS and cytochromes are more prone to adsorb onto Hem {001} nanoplate through electrostatic attraction (Hu et al., 2020; Sokolov et al., 2001). Therefore, Hem {001} nanoplates were more favorable for reduction than Hem {100} nanorods in the present study. The Fe coordination environments on different crystal facets are different, which can dominate the binding mode and electron transfer efficiency of Fe(II) on the hematite surface (Catalano et al., 2010; Rosso et al., 2010; Wu et al., 2021). Although the interactions between Fe(III)-reducing bacteria and crystal facets are complicated (Bose et al., 2009; Malvankar and Lovley, 2012; Reguera et al., 2005), the different Fe coordination environments on hematite facets might contribute to the facet-preferential reduction during DIR process.

Furthermore, this inherent difference in reducibility between two hematite nanocrystals can be ascribed to their unique surface atomic arrangements (Bai et al., 2020; Han et al., 2021). Hem {100} nanorod exhibited a concave-convex topography with the width of the grooves being only 4.559 Å (Han et al., 2021). Since the width of the groove is too small, the concave Fe(III) sites on Hem {100} nanorod are inaccessible to electron donors for microbial respiration through direct cell-mineral contacts (Lower et al., 2007; Lower et al., 2009; Madej et al., 2014). In comparison, all surface Fe(III) sites on Hem {001} nanoplate are accessible to electron donors during microbial Fe reduction, as Hem {001} nanoplate is exposed as a flat plane. Therefore, both ligand-bound conformation and steric effects are more beneficial for reduction of Hem {001} nanoplate relative to Hem {100} nanorod. Therefore, we concluded that the more reduction localized on the facet with higher biogeochemical reactivity (i.e., facet-preferential reduction) in the facet-combined system, which is obviously different from that in the facet-separate system. In especial, we found 1.8 times higher reduction degree of Hem {001} nanoplate relative to Hem {100} nanorod when the facets combined, whereas that was only 1.2 time higher when the facets ware separate.

3.4. Effects of mixing proportions and AQDS on microbially mediated reduction

To evaluate the effects of mixing proportion of two hematite nanocrystals on the microbial Fe reduction when the facets combined, we inoculated the mixture of both isotope-labeled hematite nanocrystals with varying mass ratios of [56]Hem {001} nanoplate/[NA]Hem {100} nanorod in the presence of AQDS. The amounts of Fe atoms reduced
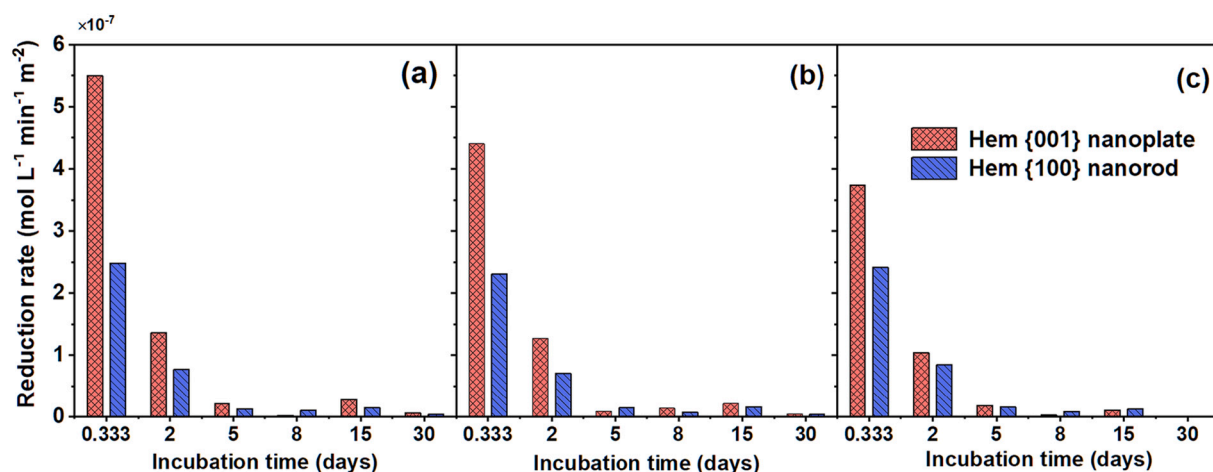
Fig. 5. Surface-area-normalized instantaneous rate of microbial Fe(III) reduction of Hem {001} nanoplate and Hem {100} nanorod in the mixture with mixing proportions of Hem {001} nanoplate/Hem {100} nanorod.

from Hem {001} nanoplate and Hem {100} nanorod were calculated based on the ^{57}Fe abundance (Fig. S11 and Table S6) and the total Fe(II) amount. After inoculation for 30 days, 39%, 62%, and 78% of Fe atoms in total Fe(II) fraction originating from Hem {001} nanoplate were observed in the incubations with 0.5, 1, and 2 of mixing proportions, respectively (Fig. S12 and Table S7). The increases in the mixing proportion (mass ratios of Hem {001} nanoplate/Hem {100} nanorod) led to an increase in the Fe atoms originating from Hem {100} nanorod. Furthermore, time-dependent reduction rates (calculated from t = i to t = i + 1) of Fe atoms for both hematite nanocrystals normalized by surface area were calculated (Fig. 5). The initial Fe(III) reduction rate were 5.5, 4.4, and 3.7 $\times 10^{-7}$ mol L^{-1} min^{-1} m^{-2} for Hem {001} nanoplate, and 2.5, 2.3, 2.4 $\times 10^{-7}$ mol L^{-1} min^{-1} m^{-2} for Hem {100} nanorod in the incubations with 0.5, 1, and 2 mixing proportions. It should be noted that change the mixing proportions of hematite nanocrystals might induce variations of both BET and surficial reaction sites of the mixture. However, Hem {001} nanoplate had a faster reduction rate than Hem {100} nanorod in all treatments. Therefore, mixing proportions of two hematite nanocrystals appear to have no apparent effects on the reduction rate of each hematite nanocrystal.

The kinetics of total Fe(II) reduced from Hem {001} nanoplate and Hem {100} nanorod by *Shewanella oneidensis* MR-1 were monitored with or without AQDS (Fig. S13). The ratio of Fe(II) to the total iron in noninoculated reactors (control treatments) was below 0.3% throughout the experiments (Fig. S13, dashed line). When AQDS was added as an electron shuttle, the extents of Fe(III) reduction of the two hematite nanocrystals were greater than those without AQDS, which is consistent with previous studies (Cutting et al., 2009; Zachara et al., 2011). In the presence of AQDS, the initial reduction rate of Fe(III) from Hem {001} nanoplate at 8 h was 7.9 $\times 10^{-7}$ mol L^{-1} min^{-1} m^{-2} and that from Hem {100} nanorod was 2.9 $\times 10^{-7}$ mol L^{-1} min^{-1} m^{-2}. In the absence of AQDS, the initial Fe(III) reduction rate was 0.72 $\times 10^{-7}$ mol L^{-1} min^{-1} m^{-2} for Hem {001} nanoplate and 0.38 $\times 10^{-7}$ mol L^{-1} min^{-1} m^{-2} for Hem {100} nanorod. In both cases, the initial Fe reduction rates of Hem {001} nanoplate were almost 2 times higher than that of Hem {100} nanorod. Therefore, facet-preferential reduction of hematite nanocrystals is independent of whether the electron transforms through direct cell-mineral contacts or electron shuttles, i.e., AH$_2$QDS.

4. Conclusions

The microbially mediated reduction of Fe(III) oxides is one of the most important biogeochemical processes on Earth's surface and significantly impacts the fate and bioavailability of vital elements and pollutants (Roden et al., 2010; Shi et al., 2020; Shi et al., 2012; Weihe

et al., 2019). In the present study, the isotope-labeled hematite facets were prepared using isotopic tracers to track iron provenance during DIR processes. Based on the results of Fe isotope tracer, the initial and final fractions of Fe(II) produced by the preferential reduction of Hem {001} nanoplates to total reduced Fe(II) were ~ 72% and ~ 63%, respectively. Our results, for the first time, demonstrated the reduction degree of Hem {001} nanoplate relative to Hem {100} nanorod (1.8 times higher) was greater than that expected by simple linear addition of separate reactors (1.2 times higher). Moreover, the *k* values of reduced Fe(II) were 3.2 $\times 10^{-2}$ d^{-1} for Hem {001} nanoplates and 2.0 $\times 10^{-2}$ d^{-1} for Hem {100} nanorods in the facet-combined system. Our findings illustrate that, in facet-combined system, the differences in reduction efficiency between different crystal facets have been underestimated because more reduction is localized on the crystal facet with stronger reactivity. Changes of the surface of Fe minerals can change their availability to environmental pollutants (Cornell and Schwertmann, 2004; Huang et al., 2018). In this work, facet-preferential reduction can result in the differences in corrosion efficiency of varying crystal facets, which strongly impact the adsorption capability and reactivity of crystal facets through changing the surface areas and adsorption sites (Cornell and Schwertmann, 2004; Notini et al., 2019; Roden and Zachara, 1996). The results of present study provide an insight into the availability and reactivity of varying crystal facets to vital elements and pollutants in soils and sediments. Overall, this work promotes our understanding of the interactive and interdependent relations between different exposed facets and helps us to clarify the biogeochemical behaviors of Fe oxide at mineral-water interfaces and the overall role of Fe oxide nanocrystals in the environments.

Declaration of Competing Interest

The authors declare that they have no known competing financial interests or personal relationships that could have appeared to influence the work reported in this paper.

Data availability

Data will be made available on request.

Acknowledgments

Program (QYZDB-SSW-DQC046) of the Chinese Academy of Sciences.

Appendix A. Supplementary data

Supplementary data to this article can be found online at https://doi.org/10.1016/j.chemgeo.2022.121166.

References

Bai, Y.G., Sun, T.R., Angenent, L.T., Haderlein, S.B., Kappler, A., 2020. Electron hopping enables rapid electron transfer between quinone−/hydroquinone-containing organic molecules in microbial iron(III) mineral reduction. Environ. Sci. Technol. 54 (17), 10646–10653. https://doi.org/10.1021/acs.est.0c02521.

Baltrusaitis, J., Cwiertny, D.M., Grassian, V.H., 2007. Adsorption of sulfur dioxide on hematite and goethite particle surfaces. Phys. Chem. Chem. Phys. 9 (41), 5542–5554. https://doi.org/10.1039/b709167b.

Barton, L.E., Quicksall, A.N., Maurice, P.A., 2012. Siderophore-mediated dissolution of hematite (alpha-Fe2O3): Effects of nanoparticle size. Geomicrobiol J. 29 (4), 314–322. https://doi.org/10.1080/01490451.2011.558566.

Boschker, H.T.S., Middelburg, J.J., 2002. Stable isotopes and biomarkers in microbial ecology. FEMS Microbiol. Ecol. 40 (2), 85–95. https://doi.org/10.1111/j.1574-6941.2002.tb00940.x.

Bose, S., et al., 2009. Bioreduction of hematite nanoparticles by the dissimilatory iron reducing bacterium Shewanella oneidensis MR-1. Geochim. Cosmochim. Acta 73 (4), 962–976. https://doi.org/10.1016/j.gca.2008.11.031.

Carbone, C., et al., 2005. Genetic evolution of nanocrystalline Fe oxide and oxyhydroxide assemblages from the Libiola mine (eastern Liguria, Italy): Structural and microstructural investigations. Eur. J. Mineral. 17 (5), 785–795. https://doi.org/10.1127/0935-1221/2005/0017-0785.

Catalano, J.G., Fenter, P., Park, C., Zhang, Z., Rosso, K.M., 2010. Structure and oxidation state of hematite surfaces reacted with aqueous Fe(II) at acidic and neutral pH. Geochim. Cosmochim. Acta 74 (5), 1498–1512. https://doi.org/10.1016/j.gca.2009.12.018.

Chan, J.Y.T., et al., 2015. Heterogeneous photo-Fenton reaction on hematite (alpha-Fe2O3){104}, {113} and {001} surface facets. Phys. Chem. Chem. Phys. 17 (38), 25333–25341. https://doi.org/10.1039/c5cp03332b.

Chanda, P., Amenabar, M.J., Boyd, E.S., Beard, B.L., Johnson, C.M., 2021. Stable Fe isotope fractionation during dissimilatory Fe(III) reduction by a thermoacidophile in acidic hydrothermal environments. Geochim. Cosmochim. Acta 292, 427–451. https://doi.org/10.1016/j.gca.2020.09.025.

Chen, L., et al., 2010. Continuous shape- and spectroscopy-tuning of hematite nanocrystals. Inorg. Chem. 49 (18), 8411–8420. https://doi.org/10.1021/ic100919a.

Colombo, C., Palumbo, G., He, J.Z., Pinton, R., Cesco, S., 2014. Review on iron availability in soil: Interaction of Fe minerals, plants, and microbes. J. Soils Sediments 14 (3), 538–548. https://doi.org/10.1007/s11368-013-0814-z.

Cornell, R.M., Schwertmann, U., 2004. The iron Oxides: Structure, Properties, Reactions, Occurences and Uses, second edition. John Wiley & Sons.

Crosby, H.A., Johnson, C.M., Roden, E.E., Beard, B.L., 2005. Coupled Fe(II)-Fe(III) electron and atom exchange as a mechanism for Fe isotope fractionation during dissimilatory iron oxide reduction. Environ. Sci. Technol. 39 (17), 6698–6704. https://doi.org/10.1021/es0505346.

Cutting, R.S., Coker, V.S., Fellowes, J.W., Lloyd, J.R., Vaughan, D.J., 2009. Mineralogical and morphological constraints on the reduction of Fe(III) minerals by Geobacter sulfurreducens. Geochim. Cosmochim. Acta 73 (14), 4004–4022. https://doi.org/10.1016/j.gca.2009.04.009.

Echigo, T., Monsegue, N., Aruguete, D.M., Murayama, M., Hochella Jr., M.F., 2013. Nanopores in hematite (alpha-Fe2O3) nanocrystals observed by electron tomography. Am. Mineral. 98 (1), 154–162. https://doi.org/10.2138/am.2013.4120.

Eggleston, C.M., Khare, N., Lovelace, D.M., 2006. Cytochrome c interaction with hematite (alpha-Fe2O3) surfaces. J. Electron Spectrosc. Relat. Phenom. 150 (2–3), 220–227. https://doi.org/10.1016/j.elspec.2005.06.006.

Frierdich, A.J., et al., 2015. Iron atom exchange between hematite and aqueous Fe(II). Environ. Sci. Technol. 49 (14), 8479–8486. https://doi.org/10.1021/acs.est.5b01276.

Furukawa, Y., Dale, J.R., 2013. The surface properties of Shewanella putrefaciens 200 and S. oneidensis MR-1: the effect of pH and terminal electron acceptors. Geochem. Trans. 14 https://doi.org/10.1186/1467-4866-14-3.

Han, R., Lv, J., Zhang, S., Zhang, S., 2021. Hematite facet-mediated microbial dissimilatory iron reduction and production of reactive oxygen species during aerobic oxidation. Water Res. 195 https://doi.org/10.1016/j.watres.2021.116988.

Handler, R.M., Beard, B.L., Johnson, C.M., Scherer, M.M., 2009. Atom exchange between aqueous Fe(II) and goethite: an Fe isotope tracer study. Environ. Sci. Technol. 43 (4), 1102–1107.

Handler, R.M., et al., 2014. Fe(II)-catalyzed recrystallization of goethite revisited. Environ. Sci. Technol. 48 (19), 11302–11311. https://doi.org/10.1021/es503084u.

Hochella, M.F., 2013. Standing back and looking at the forest: a perspective on surface and interfaces, the ubiquitous stuff of nearly all things. Elements 9 (3), 171–172.

Hu, S., et al., 2020. Facet-dependent reductive dissolution of hematite nanoparticles by Shewanella putrefaciens CN-32. Environmental Science-Nano 7 (9), 2522–2531. https://doi.org/10.1039/d0en00555j.

Hu, S., Wu, Y., Shi, Z., Li, F., Liu, T., 2021. Quinone-mediated dissimilatory iron reduction of hematite: Interfacial reactions on exposed {001} and {100} facets. J. Colloid Interface Sci. 583, 544–552. https://doi.org/10.1016/j.jcis.2020.09.074.

Huang, X., Hou, X., Song, F., Zhao, J., Zhang, L., 2016. Facet-dependent Cr(VI) adsorption of hematite nanocrystals. Environ. Sci. Technol. 50 (4), 1964–1972. https://doi.org/10.1021/acs.est.5b05111.

Huang, X., et al., 2017a. Ascorbate-promoted surface iron cycle for efficient heterogeneous Fenton alachlor degradation with hematite nanocrystals. ACS Appl. Mater. Interfaces 9 (10), 8751–8758. https://doi.org/10.1021/acsami.6b16600.

Huang, X., Hou, X., Song, F., Zhao, J., Zhang, L., 2017b. Ascorbate induced facet dependent reductive dissolution of hematite nanocrystals. J. Phys. Chem. C 121 (2), 1113–1121. https://doi.org/10.1021/acs.jpcc.6b09281.

Huang, X., Hou, X., Zhang, X., Rosso, K.M., Zhang, L., 2018. Facet-dependent contaminant removal properties of hematite nanocrystals and their environmental implications. Environmental Science-Nano 5 (8), 1790–1806. https://doi.org/10.1039/c8en00548f.

Jiang, S.Q., et al., 2020. Adsorption of Cr(VI) on Al-substituted hematites and its reduction and retention in the presence of Fe2+ under conditions similar to subsurface soil environments. J. Hazard. Mater. 390 https://doi.org/10.1016/j.jhazmat.2019.122014.

Johnson, C.M., Roden, E.E., Welch, S.A., Beard, B.L., 2005. Experimental constraints on Fe isotope fractionation during magnetite and Fe carbonate formation coupled to dissimilatory hydrous ferric oxide reduction. Geochim. Cosmochim. Acta 69 (4), 963–993. https://doi.org/10.1016/j.gca.2004.06.043.

Joshi, P., Fantle, M.S., Larese-Casanova, P., Gorski, C.A., 2017. Susceptibility of goethite to Fe2+−catalyzed recrystallization over time. Environ. Sci. Technol. 51 (20), 11681–11691. https://doi.org/10.1021/acs.est.7b02603.

Kappler, A., et al., 2021. An evolving view on biogeochemical cycling of iron. Nat. Rev. Microbiol. 19 (6), 360–374. https://doi.org/10.1038/s41579-020-00502-7.

Kerisit, S., 2011. Water structure at hematite-water interfaces. Geochim. Cosmochim. Acta 75 (8), 2043–2061. https://doi.org/10.1016/j.gca.2011.01.026.

Larsen, O., Postma, D., Jakobsen, R., 2006. The reactivity of iron oxides towards reductive dissolution with ascorbic acid in a shallow sandy aquifer - (Romo, Denmark). Geochim. Cosmochim. Acta 70 (19), 4827–4835. https://doi.org/10.1016/j.gca.2006.03.027.

Li, Z., et al., 2009. Direct hydrothermal synthesis of single-crystalline hematite nanorods assisted by 1,2-propanediamine. Nanotechnology 20 (24). https://doi.org/10.1088/0957-4484/20/24/245603.

Liu, J., et al., 2016. Particle size effect and the mechanism of hematite reduction by the outer membrane cytochrome OmcA of Shewanella oneidensis MR-1. Geochim. Cosmochim. Acta 193, 160–175. https://doi.org/10.1016/j.gca.2016.08.022.

Liu, J., Inoue, S., Zhu, R., He, H., Hochella Jr., M.F., 2021. Facet-specific oxidation of Mn (II) and heterogeneous growth of manganese (oxyhydr)oxides on hematite nanoparticles. Geochim. Cosmochim. Acta 307, 151–167. https://doi.org/10.1016/j.gca.2021.05.043.

Lower, B.H., et al., 2007. Specific bonds between an iron oxide surface and outer membrane cytochromes MtrC and OmcA from Shewanella oneidensis MR-1. J. Bacteriol. 189 (13), 4944–4952. https://doi.org/10.1128/jb.01518-06.

Lower, B.H., et al., 2009. Antibody recognition force microscopy shows that outer membrane cytochromes OmcA and MtrC are expressed on the exterior surface of *shewanella oneidensis* MR-1. Appl. Environ. Microbiol. 75 (9), 2931–2935. https://doi.org/10.1128/aem.02108-08.

Luetzenkirchen, J., et al., 2013. Surface potential at the hematite (001) crystal plane in aqueous environments and the effects of prolonged aging in water. Geochim. Cosmochim. Acta 120, 479–486. https://doi.org/10.1016/j.gca.2013.06.042.

Luo, H.-W., Zhang, X., Chen, J.-J., Yu, H.-Q., Sheng, G.-P., 2017. Probing the biotransformation of hematite nanoparticles and magnetite formation mediated by Shewanella oneidensis MR-1 at the molecular scale. Environmental Science-Nano 4 (12), 2395–2404. https://doi.org/10.1039/c7en00767a.

Lv, J., Miao, Y., Huang, Z., Hang, R., Zhang, S., 2018. Facet-mediated adsorption and molecular fractionation of humic substances on hematite surfaces. Environ. Sci. Technol. 52 (22), 13662. https://doi.org/10.1021/acs.est.8b05875.

Mackrodt, W.C., Davey, R.J., Black, S.N., Docherty, R., 1987. The morphology of α-Al2O3 and α-Fe2O3 : The importance of surface relaxation. J. Cryst. Growth 80 (2), 441–446. https://doi.org/10.1016/0022-0248(87)90093-5.

Madej, T., et al., 2014. MMDB and VAST+: tracking structural similarities between macromolecular complexes. Nucleic Acids Res. 42 (D1), D297–D303. https://doi.org/10.1093/nar/gkt1208.

Malvankar, N.S., Lovley, D.R., 2012. Microbial nanowires: a new paradigm for biological electron transfer and bioelectronics. Chemsuschem 5 (6), 1039–1046. https://doi.org/10.1002/cssc.201100733.

Mei, H.Y., et al., 2020. U(VI) adsorption on hematite nanocrystals: Insights into the reactivity of {001} and {012} facets. J. Hazard. Mater. 399 https://doi.org/10.1016/j.jhazmat.2020.123028.

Melton, E.D., Swanner, E.D., Behrens, S., Schmidt, C., Kappler, A., 2014. The interplay of microbially mediated and abiotic reactions in the biogeochemical Fe cycle. Nat. Rev. Microbiol. 12 (12), 797–808. https://doi.org/10.1038/nrmicro3347.

Murray, G.C., Hesterberg, D., 2006. Iron and phosphate dissolution during abiotic reduction of ferrihydrite-boehmite mixtures. Soil Sci. Soc. Am. J. 70 (4), 1318–1327. https://doi.org/10.2136/sssaj2005.0292.

Namgung, S., Kwon, M.J., Qafoku, N.P., Lee, G., 2014. Cr(OH)3(s) oxidation induced by surface catalyzed Mn(II) oxidation. Environ. Sci. Technol. 48 (18), 10760–10768. https://doi.org/10.1021/es503018u.

Noerpel, M.R., Lee, S.S., Lenhart, J.J., 2016. X-ray analyses of lead adsorption on the (001), (110), and (012) hematite surfaces. Environ. Sci. Technol. 50 (22), 12283–12291. https://doi.org/10.1021/acs.est.6b03913.

Notini, L., et al., 2019. Mineral defects enhance bioavailability of goethite toward microbial Fe(III) reduction. Environ. Sci. Technol. 53 (15), 8883–8891. https://doi.org/10.1021/acs.est.9b03208.

Putnis, A., 2014. Why mineral interfaces matter. Science 343 (6178), 1441–1442. https://doi.org/10.1126/science.1250884.

Reddy, T.R., Frierdich, A.J., Beard, B.L., Johnson, C.M., 2015. The effect of pH on stable iron isotope exchange and fractionation between aqueous Fe(II) and goethite. Chem. Geol. 397, 118–127.

Reguera, G., et al., 2005. Extracellular electron transfer via microbial nanowires. Nature 435 (7045), 1098–1101. https://doi.org/10.1038/nature03661.

Roden, E.E., Urrutia, M.M., 2002. Influence of biogenic Fe(II) on bacterial crystalline Fe (III) oxide reduction. Geomicrobiol J. 19 (2), 209–251. https://doi.org/10.1080/01490450252864280.

Roden, E.E., Zachara, J.M., 1996. Microbial reduction of crystalline iron(III) oxides: Influence of oxide surface area and potential for cell growth. Environ. Sci. Technol. 30 (5), 1618–1628. https://doi.org/10.1021/es9506216.

Roden, E.E., et al., 2010. Extracellular electron transfer through microbial reduction of solid-phase humic substances. Nat. Geosci. 3 (6), 417–421. https://doi.org/10.1038/ngeo870.

Rosso, K.M., Yanina, S.V., Gorski, C.A., Larese-Casanova, P., Scherer, M.M., 2010. Connecting observations of hematite (alpha-Fe2O3) growth catalyzed by Fe(II). Environ. Sci. Technol. 44 (1), 61–67. https://doi.org/10.1021/es901882a.

Royer, R.A., Burgos, W.D., Fisher, A.S., Unz, R.F., Dempsey, B.A., 2002. Enhancement of biological reduction of hematite by electron shuttling and Fe(II) complexation. Environ. Sci. Technol. 36, 1939–1946.

Shi, Z., et al., 2012. Redox reactions of reduced flavin mononucleotide (FMN), riboflavin (RBF), and anthraquinone-2,6-disulfonate (AQDS) with ferrihydrite and lepidocrocite. Environ. Sci. Technol. 46 (21), 11644–11652. https://doi.org/10.1021/es301544b.

Shi, Z., et al., 2020. Quantifying microbially mediated kinetics of ferrihydrite transformation and arsenic reduction: role of the arsenate-reducing gene expression pattern. Environ. Sci. Technol. 54 (11), 6621–6631. https://doi.org/10.1021/acs.est.9b07137.

Sokolov, I., Smith, D.S., Henderson, G.S., Gorby, Y.A., Ferris, F.G., 2001. Cell surface electrochemical heterogeneity of the Fe(III)-reducing bacteria Shewanella putrefaciens. Environ. Sci. Technol. 35 (2), 341–347. https://doi.org/10.1021/es001258s.

Soltis, J.A., et al., 2017. Electron mobility and trapping in ferrihydrite nanoparticles. ACS Earth & Space Chemistry 1 (4), 216–226. https://doi.org/10.1021/acsearthspacechem.7b00030.

Tamura, H., Goto, K., Yotsuyan, T., Nagayama, M., 1974. Spectrophotometric determination of iron(II) with 1,10-phenanthroline in presence of large amounts of iron(III). Talanta 21 (4), 314–318. https://doi.org/10.1016/0039-9140(74)80012-3.

Taylor, S.D., Kovarik, L., Cliff, J.B., Rosso, K.M., 2019. Facet-selective adsorption of Fe (II) on hematite visualized by nanoscale secondary ion mass spectrometry. Environmental Science-Nano 6 (8), 2429–2440. https://doi.org/10.1039/c9en00562e.

Van Cleemput, O., 1998. Subsoils: chemo- and biological denitrification, N2O and N2 emissions. Nutr. Cycl. Agroecosyst. 52 (2–3), 187–194. https://doi.org/10.1023/a:1009728125678.

Weber, K.A., Achenbach, L.A., Coates, J.D., 2006. Microorganisms pumping iron: anaerobic microbial iron oxidation and reduction. Nat. Rev. Microbiol. 4 (10), 752–764. https://doi.org/10.1038/nrmicro1490.

Weihe, S.H.C., Mangayayam, M., Sand, K.K., Tobler, D.J., 2019. Hematite crystallization in the presence of organic matter: Impact on crystal properties and bacterial dissolution. Acs Earth and Space Chemistry 3 (4), 510–518. https://doi.org/10.1021/acsearthspacechem.8b00166.

Wolf, M., Kappler, A., Jiang, J., Meckenstock, R.U., 2009. Effects of humic substances and quinones at low concentrations on ferrihydrite reduction by geobacter metallireducens. Environ. Sci. Technol. 43 (15), 5679–5685. https://doi.org/10.1021/es803647r.

Wu, L., Beard, B.L., Roden, E.E., Kennedy, C.B., Johnson, C.M., 2010. Stable Fe isotope fractionations produced by aqueous Fe(II)-hematite surface interactions. Geochim. Cosmochim. Acta 74 (15), 4249–4265. https://doi.org/10.1016/j.gca.2010.04.060.

Wu, F., et al., 2021. Facet-specific reactivity of hematite nanocrystals during Fe(II)-catalyzed recrystallization. Chem. Geol. 580, 120640.

Yang, Y., Ma, H.X., Zhuang, J., Wang, X., 2011. Morphology-controlled synthesis of hematite nanocrystals and their facet effects on gas-sensing properties. Inorg. Chem. 50 (20), 10143–10151. https://doi.org/10.1021/ic201104w.

Yanina, S.V., Rosso, K.M., 2008. Linked reactivity at mineral-water interfaces through bulk crystal conduction. Science 320 (5873), 218–222. https://doi.org/10.1126/science.1154833.

Zachara, J.M., et al., 2011. The mineralogic transformation of ferrihydrite induced by heterogeneous reaction with bioreduced anthraquinone disulfonate (AQDS) and the role of phosphate. Geochim. Cosmochim. Acta 75 (21), 6330–6349. https://doi.org/10.1016/j.gca.2011.06.030.

Zarzycki, P., Smith, D.M., Rosso, K.M., 2015. Proton dynamics on goethite nanoparticles and coupling to electron transport. J. Chem. Theory Comput. 11 (4), 1715–1724. https://doi.org/10.1021/ct500891a.

Zong, M.R., et al., 2019. Synthesis of 2D hexagonal hematite nanosheets and the crystal growth mechanism. Inorg. Chem. 58 (24), 16727–16735. https://doi.org/10.1021/acs.inorgchem.9b02883.